Temperature gradient induced double stabilization of the evaporation front within a drying porous medium

N. Vorhauer,[1,*] E. Tsotsas,[1] and M. Prat[2]
[1]*Otto von Guericke University Magdeburg, Universitaetsplatz 2, 39106 Magdeburg, Germany*
[2]*INPT, UPS, Institut de Mécanique des Fluides de Toulouse, Université de Toulouse, 6 Allée Emile Monso, 31400 Toulouse, France and Centre National de la Recherche Scientifique, IMFT, Allée du Professeur Camille Soula, 31400 Toulouse, France*

(Received 16 February 2018; published 6 November 2018)

Drying of porous media very often occurs in the presence of significant temperature gradients because heat fluxes are imposed in many situations in order to decrease the drying time or to facilitate the moisture removal at a higher humidity of the surrounding gas phase. Here we consider the situation where the temperature increases with depth. We show from experiments with a micromodel that the temperature gradient induces the stabilization of the evaporation front within the model porous medium according to two different mechanisms occurring consecutively. The first mechanism occurs in the liquid phase and is explained by the dependence of surface tension upon temperature. This results in the preferential invasion of the warmer zones. The second mechanism occurs gas-sided due to the dependence of saturation vapor pressure upon temperature. We show that the time scales of both mechanisms are different leading to the temporary formation of distinctive phase patterns from which different periods of drying can be discriminated.

DOI: 10.1103/PhysRevFluids.3.114201

I. INTRODUCTION

Drying of porous media occurs in natural situations [1], and is a crucial step in many industrial processes [2]. Since evaporation is an endothermic process, drying very often occurs in the presence of temperature gradients developing within the porous materials. Examples from natural situations are the soil and building materials which are naturally exposed to warm air as well as solar radiation. In addition to these examples from natural situations, the development of temperature gradients is a classical feature of convective drying where the sample is in contact with a warmer external gas flow [3] or in contact drying [4], where heat is supplied to the porous sample through hot surfaces. From the engineering standpoint, a key issue is to find an optimal tradeoff between the energy consumption and the drying time. The latter is directly linked to the drying kinetics and thus the evolution of the evaporation front inside the porous material during drying. To this end, a sufficient understanding of the impact of temperature gradients on drying kinetics in nonisothermal drying processes is critical. Also, in the drying processes encountered in many natural or engineering situations, the liquid phase contains dissolved species, i.e., dissolved salts [5], polymers [6], or particles such as in colloidal suspensions [7]. Control of the final distribution of these species after drying can be essential. For instance, in the case of salts, the drying process leads to the formation of salt crystals either within the porous medium [8,9] or on its surface [10]. This in turn can greatly affect the drying process depending on the properties of the crystallized salt layers [10]. The experimental results reported

*Corresponding author: nicole.vorhauer@ovgu.de

in [11,12] suggest that the crystals form at the evaporation front. As a result, understanding the evolution of the evaporation front during drying is a key aspect in this context.

In the classical phenomenological description of drying [13], the evaporation front is within the porous medium over the longest period of drying. This period, referred to as the receding front period (RFP) in the literature [13], is characterized by the development of a growing dry zone adjacent to the open surface of the porous medium and traveling of the internal evaporation front deeper and deeper into the porous medium. The increasing distance of the evaporation front from the open surface induces growing mass (and heat) transfer resistances, which finally leads to the deterioration of the drying performance with longer duration of this period. Consequently, a shortening of the RFP can be beneficial to industrial drying applications. In contrast with this classical description, we show in this paper that the internal evaporation front can be stabilized within the porous medium in presence of a positive temperature gradient (by convention *positive* means that the temperature increases with depth from the open surface). This is also an indirect indication that the transport of dissolved species and the localization of the crystallization zones can be greatly affected by the presence of temperature gradients.

Since the nineties, significant improvements in the understanding of drying processes have been achieved within the framework of immiscible two-phase flow theory [14]. Basic investigation tools in this context are model porous media, such as quasi-two-dimensional networks of interconnected channels [15,16], and pore network models (PNMs) (see [17,18] and references therein), with the invasion percolation theory and its variants [19,20], as theoretical background [21–23]. Application of PNMs has already led to numerous advances in our understanding of the drying process (see, for instance, [17,18,23,24] and references therein). In particular, this has led to the identification of three main patterns of the pore scale liquid distribution during drying. These depend on the existence and the sign of a gradient in the occupation probability of the pores (throats or bonds in the percolation theory) by the gas phase and are, namely, invasion percolation (IP), invasion percolation in a stabilizing gradient (IPSG), and invasion percolation in a destabilizing gradient (IPDG). One can refer to [15] for visualizations of these three patterns in a model porous medium where the case $B = 0$ corresponds to IP, $B > 0$ corresponds to IPSG, and $B < 0$ corresponds to IPDG [with bond number $B = \rho g r^2/(2\sigma \cos\theta)$, where σ is the interfacial tension, ρ is the liquid density, r the mean pore radius, g is the acceleration of gravity, and θ is the contact angle (Table I); it describes the relative importance of gravity over capillary forces]. In the IP drying regime, an expanding two-phase zone develops over the whole porous medium. In the IPSG drying regime the traveling two-phase zone is confined within the medium owing to the stabilization imposed by the hydrostatic pressure gradient. In contrast, in the IPDG drying regime an early breakthrough of the gas phase with initiation of a second front is observed. In this drying regime, the liquid phase is completely fragmented leading to a two-phase zone which remains connected to the open surface over the longest period of drying.

However, somewhat surprisingly—since the presence of temperature gradients is very frequent in drying applications—most of these works consider quasi-isothermal drying situations in which the temperature is spatially uniform and constant during the drying process. Nevertheless, the influence of temperature gradients is addressed in a limited number of papers [25–31]. In [15], the gradient in the occupation probability leading to IPDG or IPSG patterns was due to gravity effects. As first discussed in [26] from numerical pore network (PN) simulations, temperature gradients can also result in either IPSG or IPDG patterns depending on the sign of the temperature gradient, owing to the dependence of surface tension upon temperature (at least within a sufficiently weakly disordered porous medium). This will be made clear in Sec. IV [see Eqs. (5)–(8)]. The first experimental proof of the formation of the IPSG pattern in presence of a negative temperature gradient (by convention, *negative* means that the temperature decreases with depth) can be found in [31] where a visualization experiment with a quasi-two-dimensional etched network is presented. As illustrated in [26,31], the IPSG pattern is characterized by the formation of a traveling two-phase zone in between a growing dry zone adjacent to the open side and a shrinking fully saturated liquid zone at the bottom of the PN (thus equivalent to the picture in [15] for $B > 0$). So far, no experimental study of IPDG patterns is available in the literature. Numerical studies can be found in [25,26,28]. The detailed numerical

TABLE I. List of symbols.

A	interfacial area	m^2
B	Bond number	–
D_{eff}	effective diffusion coefficient	$m^2\,s^{-1}$
h	depth of pore/throat	m
Δh_v	enthalpy of vaporization	$kJ\,kg^{-1}$
L	lattice spacing	m
M	mass	kg
$M_{\text{ev,int}}$	mass evaporated within the two-phase zone	kg
$\dot{M}$	mass flow rate	$kg\,s^{-1}$
$\dot{M}_{\text{ev},0}$	initial evaporation rate	$kg\,s^{-1}$
$\tilde{M}_v$	molar mass of vapor	$kg\,kmol^{-1}$
n	number	–
N_{CBE}	number of cluster boundary liquid elements	–
p	occupation probability	–
P	pressure	Pa
P_c	capillary pressure	Pa
P_v^*	saturation vapor pressure	Pa
r_{eff}	effective pore radius	m
$\tilde{R}$	universal gas constant	$kJ\,kmol^{-1}\,K^{-1}$
S	saturation	–
S^*	saturation of the two-phase zone	–
t	time	s
T	temperature	°C, K
V	volume	m^3
$\dot{V}$	volume flow rate	$m^3\,s^{-1}$
ΔV	specific volume change	$m^3\,kg^{-1}$
w	width of pore/throat	m
w_p	in-plane diameter of pore	m
z	space coordinate from open network side	m
	Greek symbols	
ε	porosity	–
θ	contact angle	–
ν	correlation length exponent	–
ρ_l	liquid density	$kg\,m^{-3}$
$\dot{\rho}$	phase change rate	$kg\,m^{-3}\,s^{-1}$
σ	surface tension	$N\,m^{-1}$
Σ	maximum range of throat sizes	m

investigation of the situation with a positive temperature gradient presented in [25] is highlighted here. In particular, the study indicates that a dry region can form at the bottom of the system (in addition to the dry region at the top) as a result of the diffusive transport of vapor through the two-phase zone. This transport is induced by the positive temperature gradient imposed over the PN. More clearly, vapor transport through the partially saturated zone is possible due to the dependence of saturation vapor pressure upon temperature. Also, the study indicates that the ingress of the internal evaporation front from the open surface is slowed down in this case. Consequently, the expansion of the upper dry zone is limited in this situation. However, an important phenomenon, namely, the condensation of vapor traveling from the warmer to the colder region of the two-phase zone was completely ignored in the PNM used in [25]. It may, however, be expected that the diffusion of vapor against a temperature gradient can lead to a process in which both drainage (i.e., replacement of liquid by gas in the context of drying) and imbibition (invasion of gas pores by liquid due to

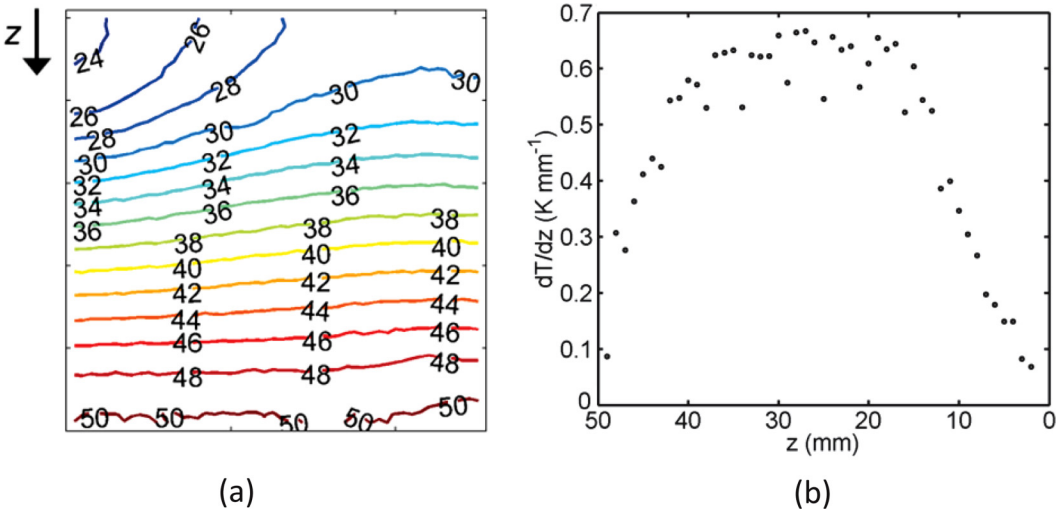

FIG. 1. (a) Temperature field with positive temperature gradient dT/dz imposed on the micromodel in the z direction. $\bar{T}_{z=0} = 24\,^{\circ}\mathrm{C}$ (top edge) and $\bar{T}_{z=49L} = 50\,^{\circ}\mathrm{C}$ (bottom edge). (b) The temperature contour lines indicate nonlinearity of the temperature gradient in the z direction.

condensation) occur simultaneously. Since imbibition invasion rules [32–36] are significantly more complex than invasion percolation rules, the simultaneous evaporation and condensation processes make the PN modeling significantly more difficult, [37,38]. In this regard, the aim of the present paper is (1) to investigate PN drying with imposed positive temperature gradient experimentally and (2) to develop a PNM taking into account the condensation phenomenon. In addition to the exploration of the ability of the developed PNM to simulate drying processes in presence of imposed thermal gradients, the PNM is also used to provide information difficult to extract from the experiment.

This paper is organized as follows. The experimental setup is presented in Sec. II and the PNM is presented in Sec. III. The experimental results are presented and discussed in Sec. IV in conjunction with some results from PN simulations. A discussion is presented in Sec. V. Conclusions are drawn in Sec. VI.

II. EXPERIMENTAL SETUP

The presented paper is based on microfluidic experiments using the quasi-two-dimensional SiO_2 micromodel and the setup described in [31]. The SiO_2 PN micromodel was produced by photolitography followed by isotropic chemical wet etching. The micromodel is a two-dimensional square network of 50 × 50 pores with one open edge (the top edge in figures presented below). The pore bodies correspond to the nodes of the network. The pores are interconnected by channels, referred to as throats or bonds. Width of the throats obeys a Gaussian distribution with mean 163.6 μm and standard deviation 15.2 μm. Width of the pores is derived from the geometry of neighbor throats; it is (171.6 ± 8.8) μm. Throats and pores have a uniform depth of 39 μm. The lattice spacing (distance between two nodes) is $L = 1$ mm. From this follows an overall size of the PN in the micromodel of 4.9 × 4.9 cm (length x width). The total void space of the PN is ≅ 28.5 μl. The microfluidic network is hydrophilic with contact angles $\theta < 45^{\circ}$.

At the beginning of the drying experiment, the micromodel was saturated with pure water and (without delay) mounted on a horizontal heat conducting plate. The temperature gradient was imposed by two thermally adjusted water streams circulating through the heat conducting plate in parallel to the open side of the micromodel. Flow direction of the water streams was from left to right (leading to the temperature distribution shown in Fig. 1). Temperature of the water streams was controlled by thermal baths. In detail, the water stream circulating at the top side of the micromodel was adjusted to a

temperature of $T \cong 5\,^{\circ}\mathrm{C}$ and the stream at the opposite side of the heat conducting plate (i.e., near the PN bottom edge) was adjusted to a temperature of $T \cong 87\,^{\circ}\mathrm{C}$. In this way, a quasi-one-dimensional temperature gradient with temperature increasing from the open surface towards the bottom of the PN could be technically realized [Fig. 1(a)]. The temperature field in Fig. 1(a) was obtained by infrared measurement; additional information was gained by continuous monitoring by thermocouples inside the heat conducting plate. The mean temperature gradient in the z direction is $dT/dz = 4.4\,\mathrm{K\,cm^{-1}}$. As depicted in Fig. 1(b), the temperature gradient is nonlinear, being higher in the center and smaller at the surface of the micromodel. Additionally, a lateral variation of temperature is observed due to the realization of heat supply with the water streams. Note that evaporative cooling was not observed. This is explained with the high heat flow rates through the thin (thickness 600 μm) silicon-cover plate of the micromodel in contact with the heat conducting plate.

A laminar flow of dry and warm air ($T_{\mathrm{air}} \cong 26\,^{\circ}\mathrm{C}$, $\dot{V}_{\mathrm{air}} = 20\,\mathrm{ml\,min^{-1}}$, and $P_{v,\mathrm{air}} \cong 0$) perpendicular to the micromodel open side [top edge in Fig. 1(a)] was applied to induce the mass transfer from the micromodel. Due to the horizontal placement of the micromodel, gravitational effects can be excluded here. Again, refer to [31] for more details and a schematic of the experimental setup.

The drying process was optically observed by a CCD camera which was installed perpendicularly above the micromodel and monitored the progressive penetration of the gas phase into it at controlled frame rates. Processing of these images after drying provides information about the decrease of liquid saturation in individual pores and throats as well as the micromodel overall liquid saturation, drying rates, or statistical parameters as will be discussed below.

III. PORE NETWORK MODEL

The proposed PNM can be regarded as a further development of the model described in [31]. The fundamental extension presented here refers to the implementation of the condensation related cluster growth mechanism. In [31] the temperature dependent direction of vapor diffusion was indeed considered, but the condensation of vapor (and the refilling of the void space by liquid) was neglected in the discussed quasi-isothermal situation and drying with negative temperature gradient. This is in contrast to the situation presented in the present paper, where the imposed positive thermal gradient leads to significant condensed liquid volume. More clearly (as it will further be discussed in Sec. IV) the net mass flow rate at the boundary of a liquid cluster can be negative in the presence of thermal gradients. This means that the overall vapor flow rate towards the cluster boundary exceeds the evaporation rate from this cluster:

$$\dot{M}_{\mathrm{cl}} = \sum_{n=1}^{N_{\mathrm{CBE}}} \dot{M}_v \tag{1}$$

(by convention, negative flow rate, $\dot{M}_{\mathrm{cl}} < 0$, means that the condensation rate is greater than the evaporation rate while positive flow rate, $\dot{M}_{\mathrm{cl}} > 0$, means that the liquid cluster is drying). As a consequence, liquid clusters can grow and reinvade neighbor throats and pores occupied by the gas phase while other clusters simultaneously shrink as a result of drying. The proposed model thus concerns the modeling of the reinvasion of pores and throats by the condensed liquid volume. This is a major improvement compared to previous PNMs of drying in presence of thermal gradients [25–31], because modeling of the liquid reinvasion implies consideration of imbibition invasion rules, [32–36], whereas the standard PNM of drying in a hydrophilic network [39] does not consider reinvasion events and therefore only applies drainage (IP) rules. For a PN like the one considered here, i.e., with pore bodies and throats of similar sizes, imbibition (refilling) rules [32] imply distinguishing pore and throat invasion as distinct events. In detail, an invasion capillary threshold is associated with each element, pore, or throat, in the network. The pistonlike displacement invasion threshold of a throat reads

$$P_{c,t} \approx \sigma\left(\frac{2}{w} + \frac{2}{h}\right) \tag{2}$$

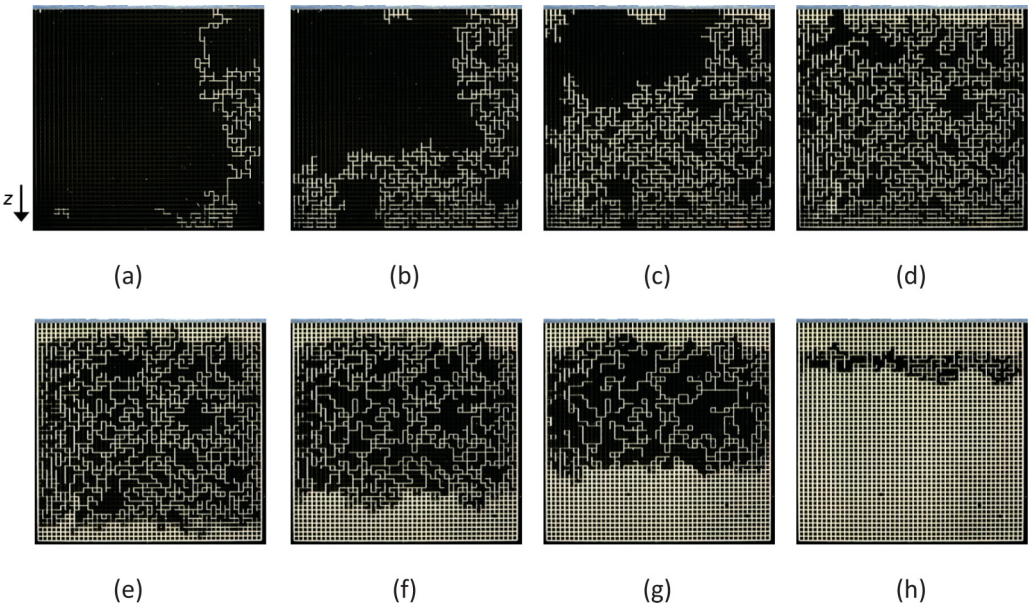

FIG. 2. Experimental phase distributions obtained from drying with $dT/dz = 0.44\,\mathrm{K\,mm^{-1}}$ and $\bar{T}_{z=0} \cong 24\,^{\circ}\mathrm{C}$. Liquid and solid in black, gas phase in light gray. Vapor escapes from top edge. Shown are the snapshots for overall network saturation $S = [0.91, 0.75, 0.57, 0.42, 0.38, 0.36, 0.34, 0.04]$, from (a) to (h), respectively.

where σ is the surface tension, w is the throat width, and h is the throat depth (Table I). This equation applies to both situations, i.e., drying or condensation inside throats. By contrast, the gas invasion threshold of a pore must be discriminated from the refilling invasion threshold of that pore. The first one can be computed from Eq. (2) while the latter is defined according to the formula proposed in [40]:

$$P_{c,p} \approx \sigma\left(\frac{1}{r_{\mathrm{eff}}} + \frac{2}{h}\right) \tag{3}$$

with

$$r_{\mathrm{eff}} = \frac{0.5 w_p}{1 + 0.25(n-1)}, \tag{4}$$

where w_p is the pore in-plane diameter and n is the number of gas throats adjacent to the considered pore.

The drying algorithm with pore and throat refilling due to condensation is summarized in the Appendix. Note that the temperature field is not computed. Instead the temperature field measured in the experiment (Fig. 1) is used as input data for the PN simulations. Note also that, within the limit of the various uncertainties in the experimental network fabrication process, a one to one correspondence between the throat sizes in the PNM and in the experimental network is imposed.

IV. RESULTS

A. Phase distributions

Figure 2 shows the gas-liquid phase distribution (patterns) obtained from a drying experiment with positive temperature gradient, with $\bar{T}_{z=0} = 24\,^{\circ}\mathrm{C}$ and $\bar{T}_{z=49L} = 50\,^{\circ}\mathrm{C}$ (Fig. 1). The images show the

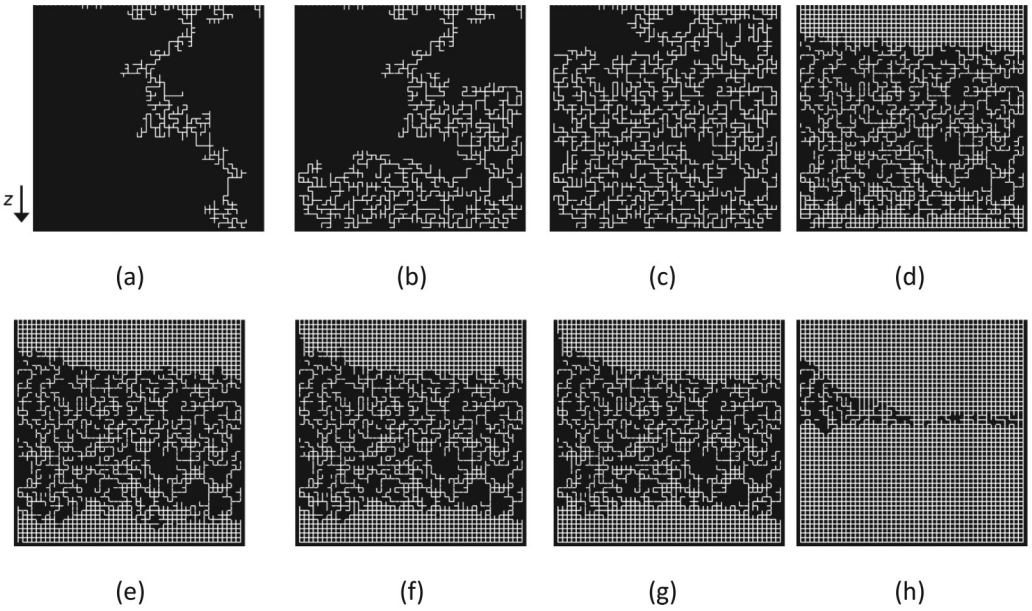

FIG. 3. PNM computed phase distributions obtained from drying with the same temperature setting as in Fig. 2. Liquid and solid in black, gas phase in white. Vapor escapes from top edge. $S = [0.91, 0.75, 0.57, 0.42, 0.38, 0.36, 0.34, 0.04]$, from (a) to (h), respectively.

distributions for decreasing overall liquid saturation S of the PN. Distributions obtained from the PN simulations are depicted in Fig. 3. In both cases (experiment and simulation) vapor escapes through the top edge where $z = 0$ while all other edges are impermeable. As can be seen from the comparison between Figs. 2 and 3, the PNM simulations lead to an evolution of the phase distribution reasonably similar to the experimental ones. Differences are, however, noticeable for low PN saturations S. These concern, namely, the distance of the liquid phase from the PN open side and the internal liquid saturation of the two-phase zone.

Several drying periods can be distinguished from the experimental phase patterns. These are precisely discussed in the following.

The first period of drying is characterized by the development of a narrow and tortuous single gas finger penetrating the micromodel starting from the open surface in the direction towards the opposite bottom edge [Fig. 2(a)]. The development of this thin finger, also referred to as the single branch, is typical of IPDG [15]. Based on the assumption of quasistatic capillary controlled invasion of the PN micromodel (viscous and gravity effects are negligible), formation of the single gas branch is explained with the dependence of surface tension upon temperature. More clearly, the gas invasion follows the path of least resistance within the micromodel. This path is dictated by the invasion capillary pressure threshold associated with each liquid element, pore, and throat [Eq. (2)].

For water (as well as for other liquids), the surface tension decreases with increasing temperature, i.e., $d\sigma/dT < 0$. For water, $d\sigma/dT \approx -1.71 \times 10^{-4}\,\mathrm{N\,m^{-1}\,K^{-1}}$. Thus the surface tension varies from approximately $72 \times 10^{-3}\,\mathrm{N\,m^{-1}}$ (cold side) to $67.8 \times 10^{-3}\,\mathrm{N\,m^{-1}}$ (hot side) over the network. As a result, the surface tension decreases with depth in our experiment. Consequently, it is comparably easier for the gas to find a throat of lower invasion threshold in the bottom region of the PN than in the colder upper region (because the pore sizes are homogenously distributed with relatively small standard deviation). This behavior can be expressed in terms of invasion probability, also referred to as the occupation probability [26]. The capillary pressure P_c, defined as $P_c = P_{\mathrm{atm}} - P_l$, where P_{atm} is the gas pressure and P_l is the pressure in the liquid phase, is spatially constant at each step

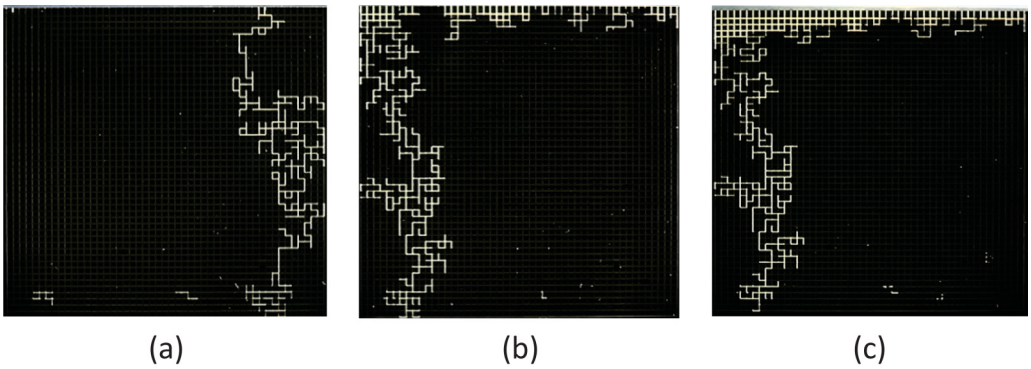

FIG. 4. Initial phase distributions observed in different experiments. (a) Experiment with temperature field as specified in Fig. 1. (b) and (c) show two experiments with reversed flow direction of water along the top edge in the heat conducting plate (the temperature field is roughly flipped from right to left).

of the invasion and corresponds to the invasion pressure threshold of the throat which is selected for invasion. Thus,

$$P_c \approx \sigma \cos\theta \left(\frac{2}{w} + \frac{2}{h} \right) = \text{const.} \tag{5}$$

Assuming here for simplicity a uniform throat width distribution in the range $[w_{t,\min},\ w_{t,\max}]$, we can express the fraction p of accessible throats corresponding to P_c as

$$p \approx \frac{w_{t,\max} - w}{\Sigma}, \tag{6}$$

where $\Sigma = w_{t,\max} - w_{t,\min}$. Thus

$$\frac{dp}{dz} = -\frac{1}{\Sigma} \frac{dw}{dz}. \tag{7}$$

Since according to Eq. (5) $w = 2[P_c/(\sigma \cos\theta) - 2/h]^{-1}$ and as σ varies spatially in the problem under study, we deduce from Eq. (7) that

$$\frac{dp}{dz} \propto -\frac{1}{\Sigma} \frac{d(\sigma \cos\theta)}{dT} \frac{dT}{dz}, \tag{8}$$

where z is the spatial coordinate directed from the open edge towards the bottom edge of the micromodel. Note that the possible variations of contact angle with temperature are neglected. Hence, in this problem, the surface tension gradient induced by the thermal gradient imposes a gradient in p. Since $d\sigma/dT < 0$, $dp/dz > 0$ when $dT/dz > 0$. The occupation probability thus increases with depth, which corresponds to an invasion percolation process in a destabilizing gradient of p (IPDG). For the analogy with the situation where gravity effects induce the gradient in the occupation probability one can refer to [15,22].

The temperature field depicted in Fig. 1(a) shows that the temperature increases along the open edge. As a result of the decrease of surface tension with increasing temperature, it is expected that the invasion starts in the warmer region of the open edge [region on the right in Fig. 1(a)]. This is indeed what is observed in Fig. 2(a). When only the cooling flow direction of the thermal bath is reversed along the top edge, the invasion starts on the left as illustrated in Figs. 4(b) and 4(c). Also, Figs. 4(b) and 4(c) illustrate that the repeatability is very good but not perfect, at least as regards the invasion of the first rows of pores. Some slight temperature variations in the top region (e.g., due to convective cooling by the drying air) are sufficient to modify the number of invaded throats in the first row before onset of the single branch development.

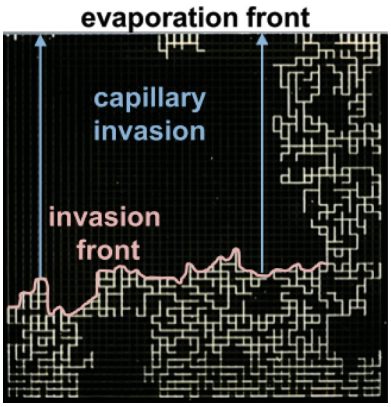

FIG. 5. Graphical representation of capillary interconnectivity. Evaporation from the top edge. The blue arrows schematically illustrate the capillary pumping effect, i.e., the invasion of the liquid cluster pinned along the evaporative top edge of the micromodel from the bottom side.

The second period of drying [Figs. 2(b)–2(d)] starts when the single branch has reached the bottom edge of the microfluidic network ($S = 0.93$). Since the occupation probability is maximum in the region of highest temperature owing to lower surface tension, the bottom region is then preferentially invaded while evaporation is from the top surface of the microfluidic PN. The preferential invasion of the bottom region is a result of the pumping effect schematically illustrated in Fig. 5.

As the result of the preferential invasion of the micromodel bottom region, a traveling invasion front sweeps the micromodel upwards [Figs. 2(b)–2(d)] until it reaches the micromodel top. At this stage, the liquid phase is completely fragmented into separated liquid clusters of various sizes forming a two-phase zone completely spanning the PN [as depicted in Fig. 2(d)]. In analogy with gravity destabilized invasion [15], it is expected that the width of the traveling front and the size of the largest cluster scale as $(dT/dz)^{-\nu/(1+\nu)}$ where ν is the correlation length critical exponent of percolation theory [41].

The third period of drying starts with the disconnection of the liquid phase from the PN top edge, i.e., with the development of a dry zone between the evaporation front and the PN top edge [Figs. 2(e)–2(g)]. The resulting diffusion resistances lead to a decrease of the overall evaporation rate (see discussions below). As a consequence, a second drying front is initiated at the high-temperature edge of the PN. It results from the preferential evaporation of liquid clusters in zones with higher temperature as well as the temperature gradient induced vapor diffusion through the two-phase zone. Traveling of this drying front from the bottom of the PN towards the open side characterizes the third period of drying. Apart from this, the position of the evaporation front in the PN upper region remains stationary. It marks the upper boundary of the two-phase zone, while the upward moving front forms the lower boundary. Accordingly, the two-phase zone is effectively shrinking while confined between a growing dry zone adjacent to the bottom and the narrower stable dry zone adjacent to the micromodel top edge. Interestingly, further study of the experimental phase patterns reveals that liquid clusters within the traveling two-phase zone are growing and merging. This is again explained with the temperature gradient induced diffusion of vapor through the two-phase zone: vapor evolving from the high-temperature boundary (bottom) flows towards the low-temperature boundary (top) which results in the condensation of vapor at the colder gas-liquid interfaces. The corresponding partial vapor pressure gradient can be expressed as

$$\frac{d \ln P_v^*}{dz} = -\frac{\Delta h_v \tilde{M}_v}{\tilde{R}} \frac{d(1/T)}{dz}, \tag{9}$$

with saturation vapor pressure P_v^* in Pa, enthalpy of evaporation Δh_v in J kg^{-1}, molar mass $\tilde{M}_v$ in kg kmol^{-1}, and ideal gas constant $\tilde{R}$ in J kmol^{-1} K^{-1}.

A fourth period of drying can be discriminated from the phase patterns in Fig. 2 and the numerical analysis presented below. In this period the upper evaporation front recedes slightly further into the PN [Fig. 2(h)].

In summary, the main periods discussed so far are as follows: period 1, characterized by development of a single gas branch; period 2, in which gas invasion sweeps upwards leading to the complete fragmentation of the liquid phase into separated clusters; period 3 with initiation of a first drying front that remains close to the open surface and a second drying front traveling upwards while growing and merging of clusters is observed; and period 4, characterized by further receding of the upper evaporation front. Invasion during both the first and the second period is capillary controlled and dictated from the temperature dependency of surface tension. During the other two periods, kinetics of vapor diffusion, evaporation, and condensation control the invasion process instead. This is studied in detail in the following section.

In the above, the possible impact of liquid films (corner menisci) [42–46] was not considered. These liquid films refer to the liquid which can remain trapped in the corners of the channels. While we have described the clusters as separated clusters, these films could help to maintain hydraulic conductivity between the various liquid clusters. These effects might explain in part the discrepancies between the experimental patterns (Fig. 2) and the computed ones (Fig. 3). Also, the liquid films might temporally maintain the hydraulic connectivity between the inside of the network and its open edge. In this case, the transition towards the third drying period would correspond to the depinning of the films from the open edge. Based on previous publications [45,46], the depinning of the films would be attributed to the thinning of them due to viscous effects. Actually, the dynamics of the corner films in the presence of a thermal gradient is an interesting problem that deserves to be studied in depth since the vapor transport in the film region is not negligible in this case, contrary to the case of the quasi-isothermal films studied in the above-mentioned references. However, it should be noted that the contact angle is expected to be on the order of $\cong 40^\circ$ in the experiments [47]. This relatively high value does not favor the development of extended liquid films [16], but, as will be shown below, the discrepancies between drying kinetics from experiments and simulation might involve liquid films and the particular structure of the liquid phase.

B. Drying kinetics

The drying curves (overall saturation as a function of time) and drying kinetics (drying rate as a function of overall saturation) of the experiment discussed in detail above are depicted in Fig. 6 together with the curves from the two experiments depicted in Figs. 4(b) and 4(c), i.e., with the same parameter setting but reversed flow direction of the water stream cooling the heat conducting plate at the surface edge of the PN. The drying kinetics are obtained from image analysis of the experimental data (also refer to Sec. II). The corresponding curves obtained from the PNM simulation are shown in Fig. 7. As can be seen, the PNM simulation again leads to results reasonably similar to the experimental ones, especially at the start of drying.

As can be seen, the drying process is characterized by two (quasi-) constant rate periods (CRPs) corresponding to a double stabilization of the evaporation front at the top and then in the upper region of the PN. Stabilization during the first CRP [$S > 0.4$ in experiments, Fig. 6(b), and $S > 0.5$ in the simulation, Fig. 7(b)] corresponds to the single gas branch development and the period referred to as the second drying period above [Figs. 2(a)–2(d)]. This stabilization effect results from the preferential invasion of the high-temperature zones already explained with the higher invasion probability induced by the temperature dependency of surface tension. It is thus an effect that is purely based on the capillary invasion of the PN. Duration of this period is around 6 to 14% of the total drying time. Drop of drying rates between the two CRPs [at $S \cong 0.4$ in experiments, Fig. 6(b), and $S \cong 0.5$ in the simulation, Fig. 7(b)] is associated with the formation of a narrow dry zone in the top rows of the PN [Figs. 2(d) and 2(e)]. It occurs after $t = 4$ h in the drying experiment from Fig. 2.

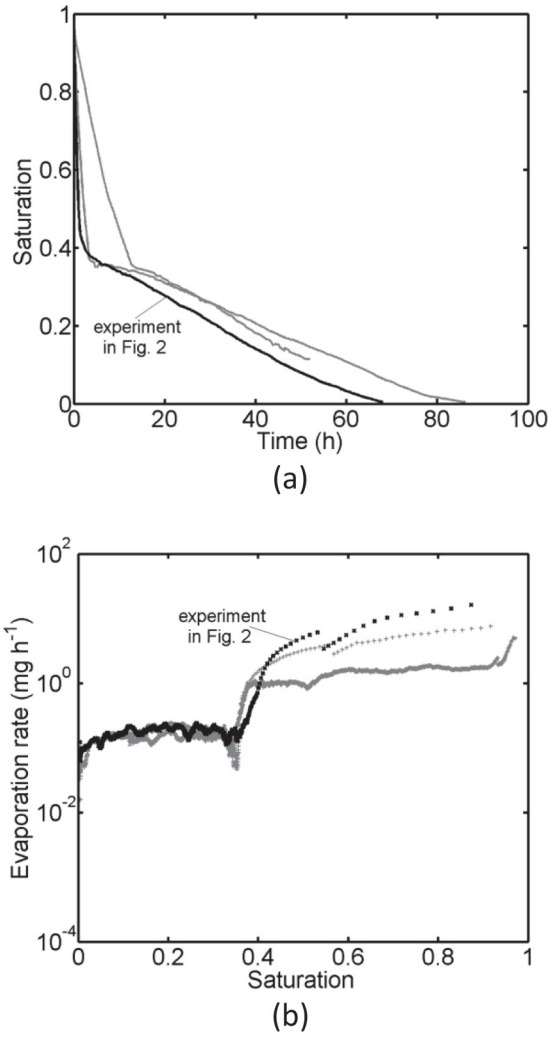

FIG. 6. Drying experiments: (a) drying curves and (b) drying rates in a semilogarithmic plot. The curves corresponding to the experiment discussed above and presented in Fig. 2 are shown in black color; experiments from Figs. 4(b) and 4(c) are shown in gray.

Stabilization during the second CRP [$S < 0.4$ in experiments, Fig. 6(b), and $S < 0.5$ in the simulation, Fig. 7(b)] corresponds to the shrinking of the two-phase zone [Figs. 2(e)–2(g)]. This period of drying is controlled by vapor diffusion and it is at least one order of magnitude longer than the fast fragmentation of the liquid phase during the first CRP. Existence of the second CRP is fully consistent with the observation that the position of the upper boundary of the two-phase zone does not appreciably change as the two-phase zone shrinks. There is, however, a drop in the evaporation rate when the two-phase zone becomes too narrow. The drop is in agreement with the observation that the evaporation front at the upper boundary of the two-phase zone slightly moves further into the PN [Fig. 2(h)]. As will be discussed in the next section, dynamics of the evaporation front is based on a ratio between vapor transport kinetics through the two-phase zone and the dry zone at the PN top edge. If the ratio is $\cong 1$, the vapor flux through the dry zone can be compensated by the vapor flux through the partially saturated zone. Then, the evaporation front remains stationary. If, however, this ratio becomes smaller than 1, then the evaporation front must

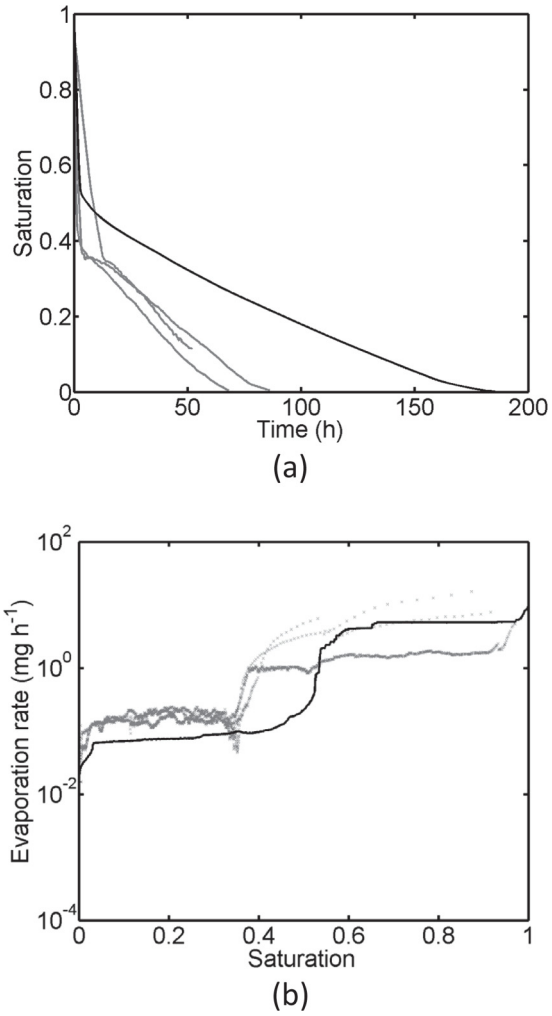

FIG. 7. PNM simulations: (a) drying curves and (b) drying kinetics. The simulated curve is shown in black and compared to the experimental data from Fig. 6, shown in gray.

travel inwards because of the negative mass balance experienced by the upper evaporation front. This is obviously linked to the width of the two-phase zone and additionally, as will be explained below, to the driving force of vapor diffusion through this zone, which is the temperature gradient in the problem discussed here.

The disagreement in drying kinetics presented in Figs. 6 and 7, i.e., after the drop of the evaporation rate, leads to an overestimation of drying time. This difference is explained with the existence of liquid films in the micromodel experiments which result in a higher interconnectivity of the liquid phase in drying periods 2–4 because they can connect the separated liquid clusters, [44]. As reported in [16] for the isothermal case, the corner films do not extend over more than one or two lattice spacings away from the liquid cluster regions in the central region of the network. The situation is somewhat different along the lateral edges of the microfluidic network. Actually liquid films develop along the right and left edges of the microfluidic device where the local geometry favors the development of liquid films over a greater distance. This has an impact on the drying kinetics since this allows for a position of the evaporation front closer to the PN surface (see also Fig. 11). It can be surmised that

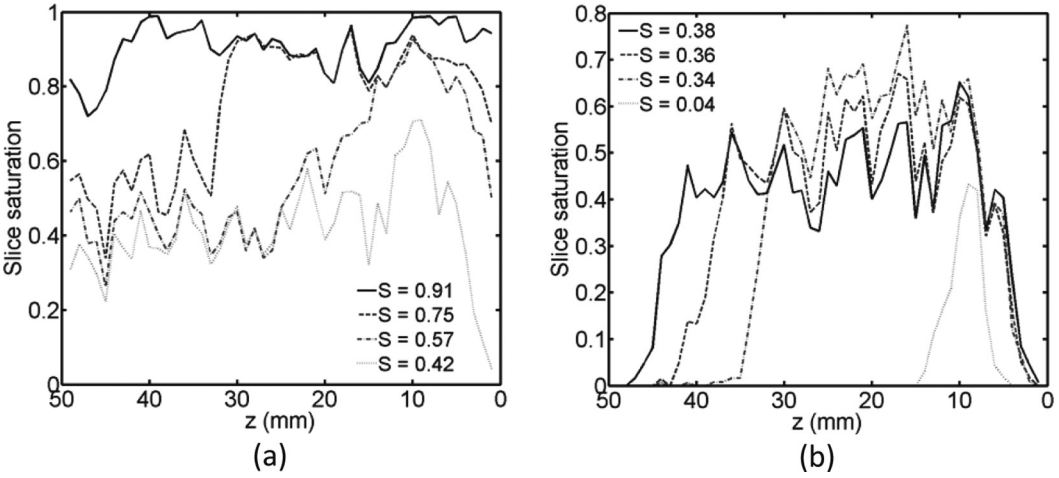

FIG. 8. Drying experiments: horizontal slice averaged saturation profiles computed from the phase distributions shown in Fig. 2. The top row corresponds to $z = 0$ mm. (a) Periods 1 and 2 up to the full fragmentation of the liquid phase. (b) Periods 3 and 4, i.e., shrinking two-phase zone. Notice the increase in slice saturation between $z \cong 8$ and 38 mm.

the situation is similar in the presence of the positive thermal gradient studied here. In addition, as already mentioned, the presence of the thermal gradient might have an impact on the film dynamics due to the vapor transport in the film region. In brief, trends regarding the possible impact of films on the drying kinetics are expected to be similar to the isothermal case with some possible additional subtleties, that deserve to be studied in future works. If the liquid interconnectivity by the lateral films is taken into account in the PNM simulation, predictability of the drying time is significantly improved. Then the simulated drying time is around 30% shorter due to a longer duration of the first constant rate period. However, the drying rate in the second CRP is still underestimated in the PNM with films, indicating that the structure of the liquid films is not well captured with this PNM. As a consequence we aim at studying more precisely the morphology of liquid films and their influence on the invasion process in drying with positive temperature gradient in future work.

C. Upper front stabilization

Comparison of Figs. 2(e)–2(g) clearly shows that reinvasions of gas pores and throats by the liquid occur within the two-phase zone in drying period 3. This is attributed to the condensation of vapor forming in the lower warmer region and traveling upwards towards the colder upper region. This is further illustrated by the slice averaged liquid saturation profiles shown in Fig. 8. As can be seen from Fig. 8(b) the slice averaged liquid saturation increases in the upper region of the two-phase zone (between $z \cong 8$ and 38 mm) in period 3. The light gray curve shows the location of residual liquid clusters at low saturations, i.e., with a noticeable distance from the micromodel open side.

The above observations in periods 3 and 4 are explained as follows. First, it should be noted that the gas phase percolates across the shrinking two-phase zone (STPZ). Second, the saturation vapor pressure P_v^* depends on temperature. Third, owing to confinement, the vapor in the throats and pores occupied by the gas phase in the STPZ is in equilibrium with the adjacent menisci, i.e.,

$$P_v(z) \approx P_v^*[T(z)]. \tag{10}$$

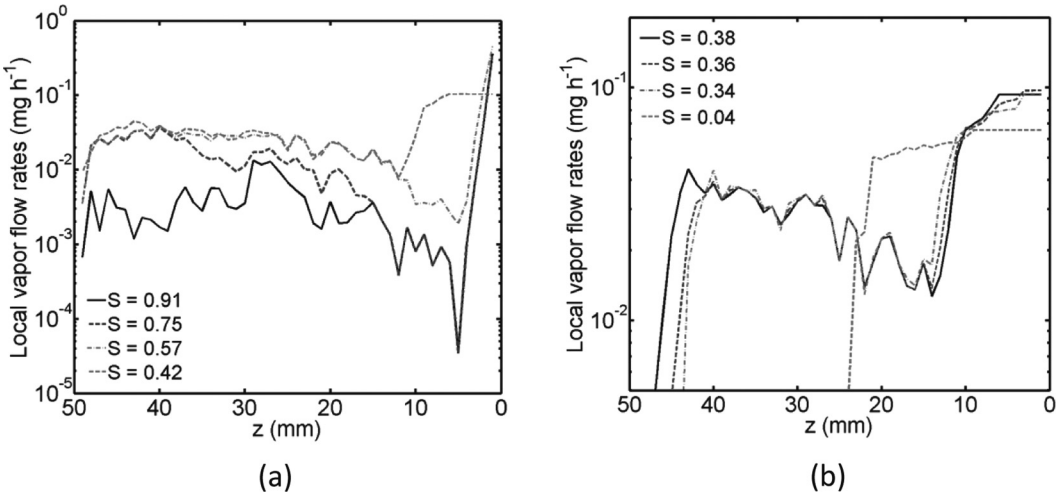

FIG. 9. PNM simulations: total through-plane vapor flow rates from the simulation corresponding to Fig. 3. The top row is located at $z = 0$ mm. Curves computed for various overall network saturation (a) $S = [0.91, 0.75, 0.57, 0.42]$ and (b) $S = [0.38, 0.36, 0.34, 0.04]$.

The vapor mass flow rate within the STPZ can thus be expressed according to a continuum approach as

$$\dot{M}_v \approx -\frac{A\tilde{M}_v}{\tilde{R}T} D_{\text{eff}} \frac{dP_v^*}{dz} \tag{11}$$

where $\tilde{M}_v$ is the vapor molecular weight, $\tilde{R}$ is the universal gas constant, A is the total cross-sectional area, and D_{eff} is the effective diffusion coefficient of vapor in the STPZ. The latter depends on the local saturation. Based on the saturation profiles depicted in Fig. 8(b), D_{eff} can be considered as approximately constant over the STPZ for simplicity. Using Eq. (9) (Clausius-Clapeyron), Eq. (11) can be expressed as

$$\dot{M}_v \approx -\frac{A\tilde{M}_v}{\tilde{R}T} D_{\text{eff}} \frac{\Delta h_v}{T\Delta V} \frac{dT}{dz}, \tag{12}$$

with specific volume change ΔV in $\text{m}^3\,\text{kg}^{-1}$.

Equation (12) indicates that the vapor flow rate in the STPZ is directed towards the top of the STPZ since $dT/dz > 0$. This is illustrated from the PN simulations in Fig. 9 where the overall through-plane mass flow rate of vapor is plotted against the slice coordinate for the overall network saturations shown in Fig. 3. The vapor flow rates are overall positive with maximum values at the PNM surface ($z \to 0$) where the vapor leaves the PN. In addition to that, curves computed for $S > 0.04$ interestingly reveal a significant drop of local vapor flow rates in slices $z \leqslant 20$ mm, i.e., in the upper part of the PN, where according to Fig. 1(b) the temperature gradient dT/dz decreases. This drop vanishes with drying of this region (i.e., the curve corresponding to the phase pattern of $S = 0.04$). These two observations, namely, (1) the drop of local vapor flow rates near the evaporation front and (2) vanishing of this drop during drying period 4, indicate that the condensation effect is primarily relevant during drying periods 1–3. However, if the plot is made dimensionless using the overall evaporation rate, it becomes clear that the mass flow rate of vapor is negligible within the micromodel before phase 3 ($S > 0.42$ in PN simulations) because vapor diffusion through the two-phase zone appears negligible compared to the overall evaporation rate from liquid clusters connected to the PN surface (Fig. 10). In agreement

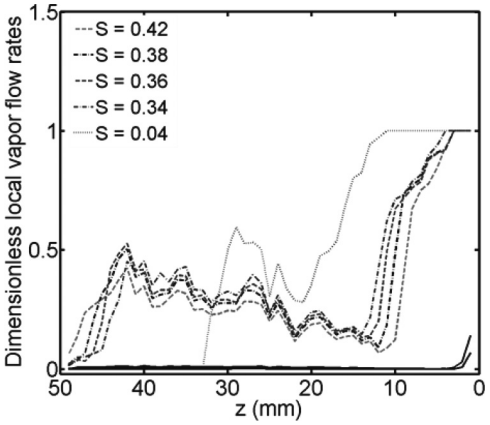

FIG. 10. PNM simulations: through-plane vapor flow rates related to overall evaporation rate. Curves highlighted in the legend of the figure correspond to period 3 and period 4 (corresponding to Fig. 3). Note that vapor flow rates are constant (with $\sum \dot{M}_v = \dot{M}_{ev}$) in the dry zone above the two-phase zone ($z \leqslant 15\,\text{mm}$). Curves for $S = [0.91, 0.75, 0.57]$ partly overlap; they are shown as solid black lines and are not distinguished by the legend.

with Fig. 7(b), where the overall drying rate drops at $S \cong 0.53$, relevance of vapor diffusion through the two-phase zone emerges below this critical saturation. In consistence with Eq. (12) and the variation of the temperature gradient dT/dz depicted in Fig. 1, the dimensionless profiles reveal again that the vapor flow rates decrease in direction towards the PN surface (curves shown for $S \leqslant 0.42$).

Considering that the transport of vapor is quasisteady, the mass conservation equation of vapor in the STPZ can be expressed according to a continuum approach as

$$\frac{d}{dz}\left(\frac{\dot{M}_v}{A}\right) = \dot{\rho}_{ev/co}, \tag{13}$$

where $\dot{\rho}_{ev/co}$ is the phase-change rate (in $\text{kg m}^{-3}\,\text{s}^{-1}$) due to evaporation ($\dot{\rho}_{ev} > 0$) or condensation ($\dot{\rho}_{co} < 0$).

Let $\bar{z}_{max}$ and $\bar{z}_{min}$ be the mean positions of the lower and upper boundary of the STPZ; the mass balance at these interfaces reads

$$\varepsilon \rho_l S^* \frac{d\bar{z}_{min}}{dt} = \frac{\tilde{M}_v}{\tilde{R}T} D_{eff}(S=0) \frac{P_v^*[T(\bar{z}_{min})]}{\bar{z}_{min}} - \frac{\tilde{M}_v}{\tilde{R}T} D_{eff}(S=S^*) \frac{dP_v^*}{dT}\frac{dT}{dz} \tag{14}$$

at $z = \bar{z}_{min}$ and

$$\varepsilon \rho_l S^* \frac{d\bar{z}_{max}}{dt} = -\frac{\tilde{M}_v}{\tilde{R}T} D_{eff}(S=S^*) \frac{dP_v^*}{dT}\frac{dT}{dz} \tag{15}$$

at $z = \bar{z}_{max}$, where S^* is the saturation of the two-phase zone (considered as constant, see Fig. 8), ε is the micromodel porosity, and ρ_l is the density of the liquid. Using again the Clausius-Clapeyron relation, Eqs. (14) and (15) can be expressed as

$$\varepsilon \rho_l S^* \frac{d\bar{z}_{min}}{dt} = \frac{\tilde{M}_v}{\tilde{R}T} D_{eff}(S=0) \frac{P_v^*[T(\bar{z}_{min})]}{\bar{z}_{min}} - \frac{\tilde{M}_v}{\tilde{R}T} D_{eff}(S=S^*) \frac{\Delta h_v}{T\Delta V}\frac{dT}{dz} \tag{16}$$

at $z = \bar{z}_{min}$ and

$$\varepsilon \rho_l S^* \frac{d\bar{z}_{max}}{dt} = -\frac{\tilde{M}_v}{\tilde{R}T} D_{eff}(S=S^*) \frac{\Delta h_v}{T\Delta V}\frac{dT}{dz} \tag{17}$$

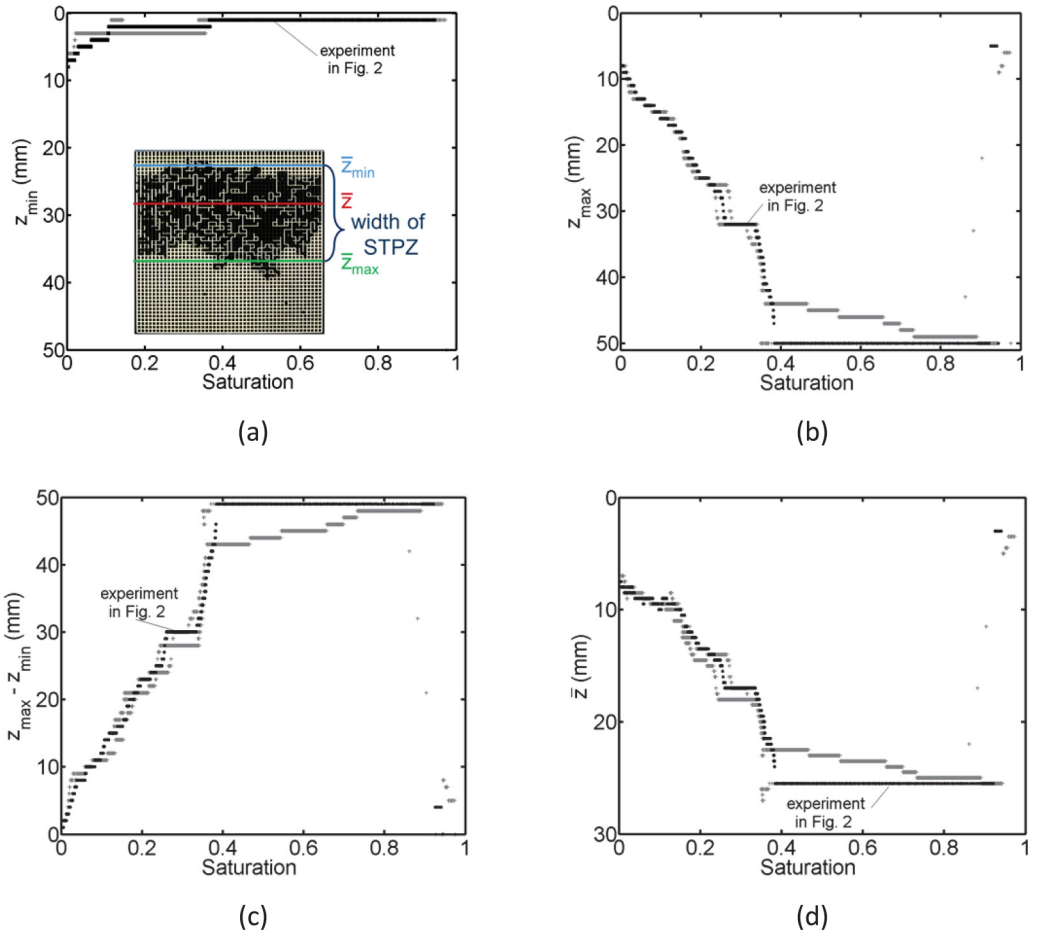

FIG. 11. (a) Upper STPZ position, (b) lower STPZ position, (c) width, and (d) mean position of STPZ obtained from the experimental patterns. Results of the experiment presented in Fig. 2 are shown in black; results from the other two experiments (Fig. 4) are shown in gray.

at $z = \bar{z}_{\max}$. According to Eq. (16), the upper front ($\bar{z}_{\min}$) can reach a stable position ($d\bar{z}_{\min}/dt \approx 0$) given by

$$\bar{z}_{\min} = \frac{D_{\text{eff}}(S=0)}{D_{\text{eff}}(S=S^*)} \frac{T\Delta V P_v^*[T(\bar{z}_{\min})]}{\Delta h_v \frac{dT}{dz}}. \tag{18}$$

Stability of this front depends on the variation of $D_{\text{eff}}(S = S^*)$, i.e., on the saturation of the two-phase zone near the front. Since this variation is weak (as indicated in Fig. 8), the position of the front is expected to be quite stable. This is what is indeed observed in Figs. 2(e)–2(g) and from the results reported in Fig. 11(a).

According to Eq. (17), the lower front is expected to move upward approximately linearly across the region of the micromodel where $dT/dz \approx$ const [$40 \leqslant z \leqslant 20$ mm according to Fig. 1(b)]. This is indeed what is observed in Fig. 6(a) [the network saturation varies quasilinearly with time during period 3 as shown in Fig. 6(a)] and depicted in Fig. 11(b). As a result, width of the STPZ decreases approximately linearly with time (i.e., with saturation) as shown in Fig. 11(c). This leads to the apparent linear displacement of the STPZ in the direction towards the PN surface [Fig. 11(d)].

Integrating Eq. (13) between $\bar{z}_{\min}$ and $\bar{z}_{\max}$ then yields

$$\int_{\bar{z}_{\min}}^{\bar{z}_{\max}} \dot{\rho}_{\mathrm{ev/co}}\, dz = \left[-\frac{\tilde{M}_v}{\tilde{R}T} D_{\mathrm{eff}}(S^*) \frac{dP_v^*}{dT} \frac{dT}{dz} \right]_{\bar{z}_{\max}} + \left[\frac{\tilde{M}_v}{\tilde{R}T} D_{\mathrm{eff}}(S^*) \frac{dP_v^*}{dT} \frac{dT}{dz} \right]_{\bar{z}_{\min}}. \tag{19}$$

Thus

$$\int_{\bar{z}_{\min}}^{\bar{z}_{\max}} \dot{\rho}_{\mathrm{ev/co}}\, dz = -\frac{\tilde{M}_v}{\tilde{R}T} D_{\mathrm{eff}}(S^*) \frac{\Delta h_v}{\Delta V} \left[\left(\frac{1}{T} \frac{dT}{dz} \right)_{\bar{z}_{\max}} - \left(\frac{1}{T} \frac{dT}{dz} \right)_{\bar{z}_{\min}} \right]. \tag{20}$$

In the case of our experiment, $(\frac{1}{T}\frac{dT}{dz})_{\bar{z}_{\max}} - (\frac{1}{T}\frac{dT}{dz})_{\bar{z}_{\min}} > 0$ (Fig. 1). Thus $\int_{\bar{z}_{\min}}^{\bar{z}_{\max}} d\dot{\rho}_{\mathrm{ev/co}} dz < 0$. As a consequence, a net condensation rate must be observed in the STPZ since the liquid mass loss corresponding to the upward motion of the lower front is greater than the evaporation rate from the upper front. As can be seen from Fig. 2, this leads to the refilling of pores and throats with liquid in the STPZ. This phenomenon is also illustrated in Fig. 12, showing the increase of the slice saturation in Fig. 12(a) (for $S < 0.4$) as well as the variation of the fraction of growing and shrinking clusters in the STPZ as a function of the micromodel saturation in Fig. 12(b). Additionally, the inset in Fig. 12(b) shows the computed cluster dynamics. It is noted here that the difference between the experimental and numerical results in Fig. 12(b) is explained as follows. A cluster is detected as growing or shrinking in the experiment by comparing two images. At least one throat must have been fully emptied or refilled between the two images for labeling the cluster as shrinking or growing. As a result, a noticeable fraction of clusters is identified as stable, i.e., not growing or shrinking, with this procedure. By contrast, a cluster is labeled as growing (or emptying) in the PNM computation when the mass flow rate at the boundary of the cluster is negative (or positive). As a result and also illustrated in Fig. 12(b), all the clusters are detected as either growing or emptying with the numerical procedure (even if the growth or shrinking rate is very small). The experimental and numerical results shown in Fig. 12(b) are qualitatively in very good agreement if one regards the second CRP and the transition between the two CRPs ($S \cong 0.4$ in experiments and $S \cong 0.5$ in the simulation), where both fractions are about equal. In the first CRP, however, the condensation effect is greater in the simulation. Precisely, the fraction of shrinking clusters and growing clusters is reversed. This is assigned to the impact of liquid films which lead to a macroscopic continuum of the liquid phase in experiments whereas the emerging (smaller) liquid clusters in the PN simulation ignoring liquid films are separated [44]. While the condensation rates can be compensated in the microfluidic PN, the smaller clusters in the PN simulation experience more often a negative phase-change rate.

The oscillations of the curves in Fig. 12(b) reveal that some throats (and pores) empty and refill several times within the STPZ. From this it can be concluded that a certain amount of water evaporates several times during the drying process (typically evaporating in the lower region of STPZ, condensing in the upper region of STPZ, and then evaporating again later). This can be expressed as

$$M_{\mathrm{ev}}(t) = M_{\mathrm{ev,int}}(t) - M_{\mathrm{co}}(t), \tag{21}$$

where $M_{\mathrm{ev}}(t)$ is the mass of water that has left the system (i.e., the net evaporation), $M_{\mathrm{ev,int}}(t)$ is the mass of water that has evaporated within the system, and $M_{\mathrm{co}}(t)$ is the mass of water that has condensed within the system at time t. As can be seen from Fig. 13, the total mass of water evaporating in the network over the complete drying process is by around 20% larger than the net evaporated mass with the temperature setting and PN used in the drying simulation.

V. DISCUSSIONS

A. Liquid phase fragmentation

As depicted in Fig. 2, the liquid phase is fragmented into clusters of various sizes at the beginning of period 3, i.e., after the sweeping of the micromodel by the gas invasion events that start at the bottom of the network and move upwards. This fragmentation is a consequence of the dependence of surface tension upon temperature.

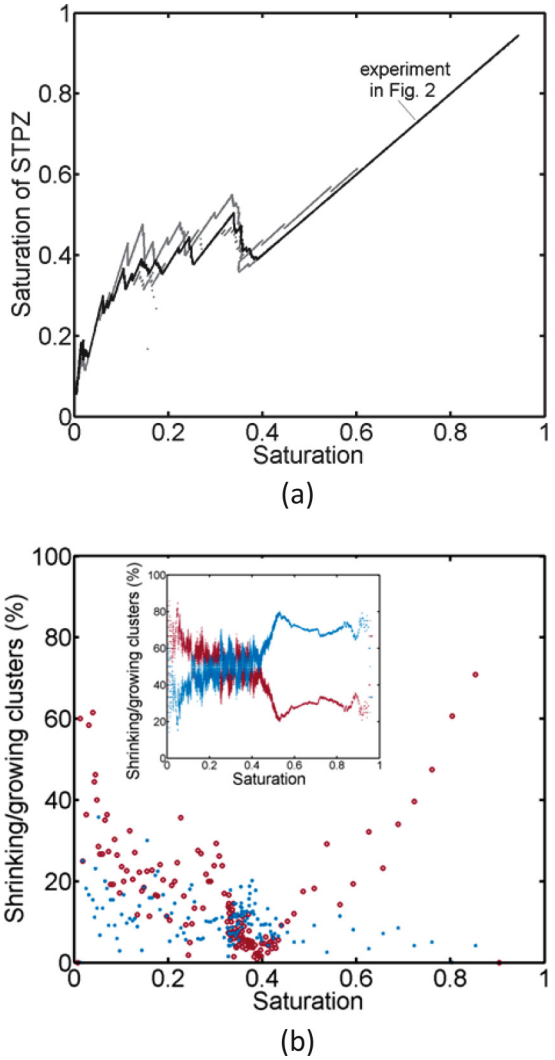

FIG. 12. (a) Saturation of the STPZ (experiment from Fig. 2 in black; additional experimental curves in gray). (b) Percentage ratio of shrinking (in red) and growing (in blue) clusters related to the current total number of clusters determined by image processing of experimental patterns (see text); the inset shows the same type of data from the PNM simulations (see text).

Interestingly, a similar fragmented liquid distribution is obtained when the effect of temperature on surface tension is neglected [25]. As discussed in [26], this should also correspond to the situations where the porous medium disorder, i.e., the standard deviation of the throat size distribution, is sufficiently large for rendering ineffective the impact of surface tension variations associated with the spatial variations in temperature [from Eq. (8), $dp/dz \to 0$ when Σ becomes large]. In other words, invasion of the PN is entirely controlled by the throat size distribution when the disorder is sufficiently large [26]. As illustrated in Fig. 14, the front of gas invasion sweeping the porous medium moves downwards in this case and the isolated clusters forming behind the front do not evaporate, or evaporate only slowly, because of the temperature gradient induced vapor flux in the two-phase zone (similarly as through the STPZ discussed in Sec. IVC). In other words, evaporation from the upper isolated clusters is compensated by the condensation flux experienced by these clusters.

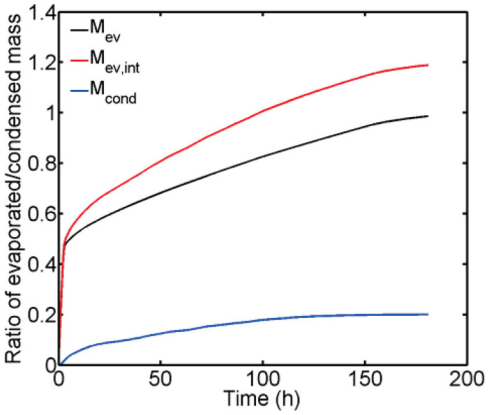

FIG. 13. PNM computation of the variation of $M_{\mathrm{ev}}(t)$ (net evaporation), $M_{\mathrm{ev,int}}(t)$, and $M_{\mathrm{co}}(t)$ [Eq. (21)] related to the initial mass of water in the PN [$M(t=0) = 0.0284\,\mathrm{g}$].

This also makes clear that the evaporation front stabilization mechanism in the second CRP discussed in Sec. IVC is not related to the dependence of surface tension upon temperature.

B. Impact of temperature gradient on upper front position

According to Eq. (18), position of the upper front in period 3 must be closer to the open side of the micromodel as the temperature gradient is increased. This is indeed what is obtained from PNM simulations as illustrated in Fig. 15. Figure 15 summarizes the results from 12 PN simulations using a PN structure identical to the microfluidic model studied above but different imposed temperature gradients and various initial evaporation rates which were adjusted by an external mass transfer

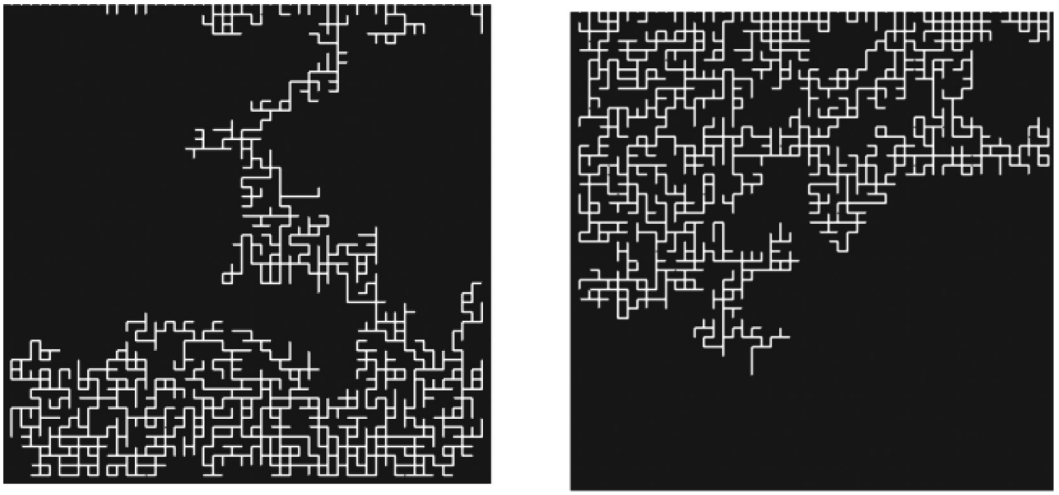

FIG. 14. Two mechanisms leading to a fragmented liquid phase spanning the network. Illustration from PNM simulations: (a) IPDG pattern with upward moving gas invasion front sweeping the network from below and (b) IP pattern with downward moving gas invasion front sweeping the system from the top and isolated liquid clusters stabilized by condensation ($S = 0.75$).

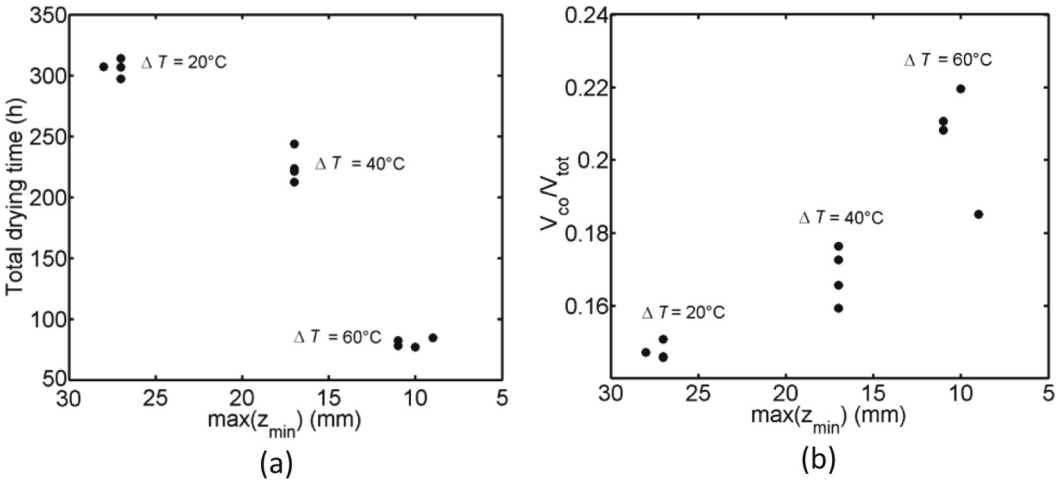

FIG. 15. Impact of the temperature gradient and the initial evaporation rate (a) on the overall drying time and (b) the total amount of condensed liquid volume from PN simulations with PN identical to the microfluidic network and different imposed thermal gradients. The initial evaporation rates vary in the range of $\dot{M}_{ev,0} = [15.7,\ 3.15,\ 1.6,\ 0.8]$ mg h^{-1} according to a variation in the thickness of the diffusive boundary layer with which the mass transfer from the PN surface is simulated (refer to [48] for more details).

coefficient [16,26,42]. As can be seen in Fig. 15, three distinct point clouds can be distinguished. Each of these point clouds refers to a different temperature setting as indicated in the figure. Variation of the intial evaporation rates (at constant ΔT) instead has a minor impact which is reflected by the density of the point clouds. Figure 15(a) clearly reveals that higher ΔT positively affects the mean upper position of the evaporation front. This leads to a drastic decrease in drying time although the ratio of the total condensed liquid volume inside the STPZ increases for higher ΔT [Fig. 15(b)]. It is concluded that the evaporation rate in the second CRP can be controlled by playing with the temperature gradient as it positively affects the position of the evaporation front.

C. Three-dimensional systems

When the temperature gradients are negligible, the drying behavior of a three-dimensional (3D) system [49] differs from that of a 2D system essentially because both the liquid and gas phase can form percolating clusters over the network during the first period of drying in a 3D system. This feature results in a CRP in 3D systems, which is typically not observed in isothermal 2D systems (an exception, however, is when film effects are very significant [18]). In the presence of a positive thermal gradient, such a difference between 2D and 3D systems is not expected when the temperature gradient is strong enough to lead to IPDG as in our experiment. Then the main periods of drying are expected to be quite similar in 2D and 3D systems. When the single branch does not form because of sufficiently strong disorder or too low temperature gradient, then of course the situation must be different between 2D and 3D simulations. As illustrated in Fig. 14(b) for drying of the 2D PN, stabilization of the evaporation front in the first drying period is due to the stabilization of clusters forming the fragmented liquid phase, whereas in the 3D case the liquid phase would form a shrinking spanning cluster in the first drying period. Thus, occurrence of the first CRP in a 3D PN with imposed positive temperature gradient is similar to isothermal drying [49]. However, later in the drying process, when the liquid phase is totally fragmented in the 3D system, the situation is not fundamentally different from the fragmented 2D case: a similar stabilization of the evaporation front is expected in both systems. This is explained with the vapor flux induced by the thermal gradient in the fragmented two-phase zone. In summary, two CRPs are generally expected to be observed in the presence of a sufficiently large positive thermal gradient but the mechanism responsible for the

occurrence of the first CRP can be different in 3D and 2D PNs when the development of the single gas branch at the beginning of drying does not occur. We plan to illustrate in more detail the 3D case from PNM simulations in a forthcoming paper.

VI. CONCLUSIONS

We have presented experimental results using a quasi-two-dimensional model porous medium with the aim to show the strong impact of a positive temperature gradient, imposed on the micromodel, on the drying process. A positive temperature gradient means that temperature increases with depth of the micromodel. We have demonstrated that the dependence of surface tension upon temperature and the dependence of saturation vapor pressure upon temperature lead to a double stabilization of the evaporation front in two consecutive periods. In the first period, the stabilization results from the impact of the temperature gradient on the invasion pattern. This changes the pattern from an IP pattern, characteristic for drying in the absence of a temperature gradient, to an IPDG pattern. In the second period, the stabilization results from the vapor flux induced through the fragmented liquid phase.

Additional insights were obtained from PNM simulations taking into account the refilling process of throats and pores due to the condensation of vapor transported through the two-phase zone. It was shown that this effect primarily affects the drying process when the liquid phase is fragmented and when additionally the overall evaporation rate from the PN surface is sufficiently low. As a result of condensation, throats and pores are locally reinvaded which leads to a considerable growth of liquid clusters. From this follows that shape of the liquid clusters is affected by the condensation of vapor. They become more faceted than one would expect from the corresponding imbibition situation. Moreover, some throats and pores can empty and refill several times during the drying process.

In this respect, it can be noted that situations in which the liquid phase is fragmented and where drainage and imbibition processes occur simultaneously are notoriously difficult to simulate with the standard continuum models of drying. Finally, the results reported in this paper open up the route for control of the drying process by playing with the temperature gradient.

Some discrepancies between the experiments and the simulations might be due to the impact of corner liquid films. These films were not considered in the model. The dynamics of those films in the presence of a thermal gradient as well as their possible role in the hydraulic connectivity between clusters deserve future study.

ACKNOWLEDGMENTS

We gratefully acknowledge production of a microfluidic device with very high precision by the Institute of Micro and Sensor Technique at Otto von Guericke University. Cooperation between the Institutes was financially supported by Deutsch-Franzoesische-Hochschule/Université franco-allemande (DFH-UFA) and Deutsche Forschungsgemeinschaft (in the framework of Graduate School Micro-Macro-Interactions in Structured Media and Particle Systems Grant No. DFG-GRK-1554).

APPENDIX

The PN drying algorithm for computation of nonisothermal drying in the presence of imposed thermal gradients is briefly described in what follows. The base of this algorithm is the PNM presented in [31]. The features of the PNM with simultaneous evaporation and condensation are highlighted below. Computation of the invasion of the PN follows IP rules assuming quasisteady invasion and negligible pressure drops due to viscous forces inside the liquid phase. Thus, the order of invasion of pores and throats, either by the gas phase or the liquid phase, is computed from analysis of the invasion capillary pressure thresholds. The invasion process is coupled to the vapor flow rates resulting from the vapor partial pressure gradient between the gas-liquid interface and the gas bulk phase in the boundary layer of the PN. In case of overall positive vapor flow rates, i.e., when the liquid cluster is drying, the pore or throat at the cluster boundary associated with the lowest capillary pressure

threshold is invaded by the gas phase. By contrast, in case of overall negative flow rates (i.e., cluster growing) the pore or throat associated with the highest capillary pressure threshold is invaded by the liquid phase. It is noted that, in case of cluster growing, at first all partially saturated elements (emerging from the cluster mass balances) are resaturated with liquid before the neighborhood of the cluster is scanned for possible empty candidates.

In summary the drying algorithm reads as follows. After initiation of the PN structure and physical parameters, the vapor pressure field inside empty network pores is computed from the mass balance of each empty pore node following Eq. (11). The boundary conditions are $P_v = P_v^*(T)$ in pores at the gas-liquid interface and $P_v = P_v^\infty = 0$ in pores connected to the bulk air phase. The invasion rate of any liquid cluster as well as of single liquid elements is computed from the sum of vapor flow rates towards and from the cluster boundary [Eq. (1)]. Care is taken to correctly determine the direction of vapor flow rates in the nonisothermal PNM.

Then, the following steps are computed. If the interfacial mass balance of the cluster is positive (i.e., the cluster is shrinking), (1) scan each liquid cluster boundary for the meniscus throat or meniscus pore with the lowest capillary pressure threshold (equivalent to the local candidate to be invaded by the gas phase) and (2) compute the time required to fully invade the local candidate with gas at the current cluster evaporation rate. This is consistent with traditional PN drying models. Additionally, the following steps are applied in the PN drying model with condensation. If the interfacial mass balance of the cluster is negative and partially saturated elements are available at the cluster boundary (i.e., resaturation of the cluster boundary), (1) scan each liquid cluster boundary for the partially saturated meniscus throats or meniscus pores with the highest capillary pressure threshold (equivalent to the local candidate to be invaded by the liquid phase) and (2) compute the time required to fully invade the local candidate with liquid at the current cluster condensation rate. If the interfacial mass balance of the cluster is negative and partially saturated elements are not available at the cluster boundary (i.e., the cluster is growing), (1) scan adjacent empty pores and throats for the local candidate with the highest entry pressure threshold (equivalent to the local candidate to be invaded by the liquid phase) and (2) compute the time required to fully invade the local candidate with liquid at the current cluster condensation rate.

Invasion pressure thresholds are computed from Eqs. (2) and (3). The invasion times are computed from

$$t = \frac{S \rho_l V}{\dot{M}_{\mathrm{ev}}} \tag{A1}$$

for gas invasion, and from

$$t = \frac{(1 - S) \rho_l V}{-\dot{M}_{\mathrm{co}}} \tag{A2}$$

for liquid invasion. Single liquid elements are treated analogously. Finally, the one candidate among all clusters and single liquid elements for which the fastest invasion time is identified is selected for invasion. This element is referred to as the global candidate and it is the only element which is fully invaded during this time step. The time interval of this invasion event is determined from Eq. (A1) or Eq. (A2) depending on the kind of invasion (i.e., either drying or condensation). Saturation of all other candidates is updated according to

$$S^t = S^{t-1} - t \frac{\dot{M}_{\mathrm{ev/co}}}{\rho_l V}, \tag{A3}$$

with saturation S at time index t and time index $t - 1$. Then cluster labeling and variables are updated before repetition of this procedure until $S = 0$.

[1] T. Kobayashi, W. He, and H. Nagai, Mechanisms of evaporation from soil with a dry surface, Hydrol. Process. **12**, 13 (1998).
[2] *Handbook of Industrial Drying*, edited by A. S. Mujumdar, 4th ed. (CRC, Boca Raton, FL, 2014).
[3] M. Ilic and I. W. Turner, Convective drying of a consolidated slab of wet porous material, Int. J. Heat Mass Tran. **32**, 2351 (1989).
[4] M. D. Mikhailov and B. K. Shishedjiev, Temperature and moisture distributions during contact drying of a moist porous sheet, Int. J. Heat Mass Tran. **18**, 15 (1975).
[5] J. Desarnaud, H. Derluyn, L. Molari, S. de Miranda, V. Cnudde, and N. Shahidzadeh, Drying of salt contaminated porous media: Effect of primary and secondary nucleation, J. Appl. Phys. **118**, 114901 (2015).
[6] A. P. A. Faiyas, S. J. F. Erich, H. P. Huinink, O. C. G. Adan, and T. G. Nijland, Effect of MHEC on evaporation and hydration characteristics of glue mortar, Cement Concrete Res. **83**, 97 (2016).
[7] E. Keita, P. Faure, S. Rodts, and P. Coussot, MRI evidence for a receding-front effect in drying porous media, Phys. Rev. E **87**, 062303 (2013).
[8] N. Sghaier, S. Geoffroy, M. Prat, H. Eloukabi, and S. B. Nasrallah, Evaporation driven growth of large crystallized salt structures in a porous medium, Phys. Rev. E **90**, 042402 (2014).
[9] M. Börnhorst, P. Walzel, A. Rahimi, A. Kharaghani, E. Tsotsas, N. Nestle, A. Besser, F. Kleine Jäger, and T. Metzger, Influence of pore structure and impregnation: Drying conditions on the solid distribution in porous support materials, Dry. Technol. **34**, 1964 (2016).
[10] H. Eloukabi, N. Sghaier, S. B. Nasrallah, and M. Prat, Experimental study of the effect of sodium chloride on drying of porous media: The crusty-patchy efflorescence transition, Int. J. Heat Mass Tran. **56**, 80 (2013).
[11] H. Derluyn, P. Moonen, and J. Carmeliet, Deformation and damage due to drying-induced salt crystallization in porous limestone, J. Mech. Phys. Solids **63**, 242 (2014).
[12] C. Noiriel, F. Renard, M.-L. Doan, and J-P. Gratier, Intense fracturing and fracture sealing induced by mineral growth in porous rocks, Chem. Geol. **269**, 197 (2010).
[13] J. Van Brakel, Mass transfer in convective drying, Adv. Drying **1**, 217 (1980).
[14] R. Lenormand, E. Touboul, and C. Zarcone, Numerical models and experiments on immiscible displacements in porous media, J. Fluid Mech. **189**, 165 (1988).
[15] J. B. Laurindo and M. Prat, Numerical and experimental network study of evaporation in capillary porous media. Phase distributions, Chem. Eng. Sci. **51**, 5171 (1996).
[16] N. Vorhauer, Y. J. Wang, A. Kharaghani, E. Tsotsas, and M. Prat, Drying with formation of capillary rings in a model porous medium, Transport Porous Med. **110**, 197 (2015).
[17] M. Prat, Recent advances in pore-scale models for drying of porous media, Chem. Eng. J. **86**, 153 (2002).
[18] M. Prat, Pore network models of drying, contact angle and films flows, Chem. Eng. Technol. **34**, 1029 (2011).
[19] D. Wilkinson and J. Willemsen, Invasion percolation: A new form of percolation theory, J. Phys. A **16**, 3365 (1983).
[20] D. Wilkinson, Percolation effects in immiscible displacement, Phys. Rev. A **34**, 1380 (1986).
[21] T. M. Shaw, Drying as an Immiscible Displacement Process with Fluid Counterflow, Phys. Rev. Lett. **59**, 1671 (1987).
[22] M. Prat and F. Bouleux, Drying of capillary porous media with a stabilized front in two dimensions, Phys. Rev. E **60**, 5647 (1999).
[23] I. N. Tsimpanogiannis, Y. C. Yortsos, S. Poulou, N. Kanellopoulos, and A. K. Stubos, Scaling theory of drying in porous media, Phys. Rev. E **59**, 4353 (1999).
[24] A. G. Yiotis, I. N. Tsimpanogiannis, A. K. Stubos, and Y. C. Yortsos, Pore-network study of the characteristic periods in the drying of porous materials, J. Colloid Interf. Sci. **297**, 738 (2006).
[25] H. P. Huinink, L. Pel, M. A J. Michels, and M. Prat, Drying processes in the presence of temperature gradients: Pore-scale modelling, Eur. Phys. J. E **9**, 487 (2002).
[26] F. Plourde and M. Prat, Pore network simulations of drying of capillary media: Influence of thermal gradients, Int. J. Heat Mass Tran. **46**, 1293 (2003).

[27] V. K. Surasani, T. Metzger, and E. Tsotsas, Consideration of heat transfer in pore network modelling of convective drying, Int. J. Heat Mass Tran. **51**, 2506 (2008).
[28] V. K. Surasani, T. Metzger, and E. Tsotsas, Influence of heating mode on drying behaviorof capillary porous media: pore scale modeling, Chem. Eng. Sci. **63**, 5218 (2008).
[29] V. K. Surasani, T. Metzger, and E. Tsotsas, A non-isothermal pore network drying model with gravity effect, Transport Porous Med. **80**, 431 (2009).
[30] V. K. Surasani, T. Metzger, and E. Tsotsas, Drying simulations of various 3D pore structures by a non-isothermal pore network model, Dry. Technol. **28**, 615 (2010).
[31] N. Vorhauer, Q. T. Tran, T. Metzger, E. Tsotsas, and M. Prat, Experimental investigation of drying in a model porous medium: Influence of thermal gradients, Dry. Technol. **31**, 920 (2013).
[32] R. Lenormand and C. Zarcone, Role of roughness and edges during imbibition in square capillaries, in *Proceedings of the SPE Annual Technical Conference and Exhibition*, SPE 13264 (SPE, 1984).
[33] M. Cieplak and M. O. Robbins, Influence of contact angle on quasi static fluid invasion of porous media, Phys. Rev. B **41**, 11508 (1990).
[34] M. J. Blunt and H. Scher, Pore-level modeling of wetting, Phys. Rev. E **52**, 6387 (1995).
[35] O. Chapuis and M. Prat, Influence of wettability conditions on slow evaporation in two-dimensional porous media, Phys. Rev. E **75**, 046311 (2007).
[36] H. Chraibi, M. Prat, and O. Chapuis, Influence of contact angle on slow evaporation in two dimensional porous media, Phys. Rev. E **79**, 026313 (2009).
[37] K. H. Le, A. Kharaghani, C. Kirsch, and E. Tsotsas, Discrete pore network modeling of superheated steam drying, Dry. Technol. **35**, 1584 (2017).
[38] A. Rahimi, T. Metzger, A. Kharaghani, and E. Tsotsas, Interaction of droplets with porous structures: Pore network simulation of wetting and drying, Dry. Technol. **34**, 1129 (2016).
[39] M. Prat, Percolation model of drying under isothermal conditions in porous media, Int. J. Multiphas. Flow **19**, 691 (1993).
[40] V. Mani and K. K. Mohanty, Effect of pore-space spatial correlations on two-phase flow in porous media, J. Petrol Sci. Eng. **23**, 173 (1999).
[41] D. Stauffer and A. Aharony, *Introduction to Percolation Theory* (Taylor & Francis, London, 1992).
[42] A. G. Yiotis, A. G. Boudouvis, A. K. Stubos, I. N. Tsimpanogiannis, and Y. C. Yortsos, Effect of liquid films on the isothermal drying of porous media, Phys. Rev. E **68**, 037303 (2003).
[43] A. G. Yiotis, A. G. Boudouvis, A. K. Stubos, I. N. Tsimpanogiannis, and Y. C. Yortsos, Effect of liquid films on the drying of porous media, AIChE J. **50**, 2721 (2004).
[44] A. G. Yiotis, D. Salin, and Y. C. Yortsos, Pore network modeling of drying processes in macroporous materials: effects of gravity, mass boundary layer and pore microstructure, Transport Porous Med. **110**, 175 (2015).
[45] F. Chauvet, P. Duru, S. Geoffroy, and M. Prat, Three Periods of Drying of a Single Square Capillary Tube, Phys. Rev. Lett. **103**, 124502 (2009).
[46] F. Chauvet, P. Duru, and M. Prat, Depinning of evaporating liquid films in square capillary tubes: Influence of corners roundness, Phys. Fluids **22**, 112113 (2010).
[47] N. Sghaier, M. Prat, and S. Ben Nasrallah, On the influence of sodium chloride concentration on equilibrium contact angle, Chem. Eng. J. **122**, 47 (2006).
[48] T. Metzger, A. Irawan, and E. Tsotsas, Isothermal drying of pore networks: Influence of friction for different pores structures, Dry. Technol. **25**, 49 (2007).
[49] Y. Le Bray and M. Prat, Three dimensional pore network simulation of drying in capillary porous media, Int. J. Heat Mass Tran. **42**, 4207 (1999).